ELSEVIER

Nuclear Instruments and Methods in Physics Research B 122 (1997) 283-292

NIM B
Beam Interactions
with Materials & Atoms

Monte Carlo study of an imager for low-energy γ-ray astronomy: Optimization of the design and evaluation of the scientific performances

F. Sánchez [a,*], F. J. Ballesteros [b], V. Reglero [b]

[a] *Instituto de Fisica Corpuscular, Universidad de Valencia CSIC, Dr. Moliner, 50, E-46100 Burjasot, Valencia, Spain*
[b] *Departamento de Astronomia y Astrofisica, Universidad de Valencia, Dr. Moliner, 50, E-46100 Burjasot, Valencia, Spain*

Received 14 May 1996; revised form received 4 October 1996

Abstract

In this paper we present the phase A studies which were carried out for the optimization of the design and evaluation of the scientific performances of the Imager, which is one of the two main instruments under development for the INTEGRAL mission, selected by ESA as the next scientific mission of medium size (M2).

These studies were done by Monte Carlo simulation, using the CERN GEANT-3 package. Both the whole geometry and materials defining the Imager were considered in the simulations.

1. Introduction

The recent satellite missions CGRO and GRANAT have made, in the last four years, a significant improvement of our knowledge of the sky at γ-ray energies (see Refs. [1-5] and references therein for a review). Many are the scientific results which have been obtained by these two experiments. It is however interesting to briefly report here the points which could have important consequences concerning the development of a future γ-ray telescope: a) the hard X- and γ-ray sources show a high degree of variability both in number and intensity; b) although the number of low energy γ-ray sources is relatively low, several regions of the sky exist (an example is the galactic centre), where the relatively high density of γ-ray objects gives rise to problems regarding both confusion and identification of these sources with objects known at other wavelengths; c) the spectrum of many among the γ-ray sources indicates the presence of several features which also show a high degree of intensity variability.

These points translate into the two key requirements for a future γ-ray mission: i) imaging capability with good angular resolution ($< 30'$ at 1 MeV) within a large field of view to allow the accurate positioning of the detected point sources, and to study the morphology of the diffuse emission regions; ii) fine spectroscopy capability over a large energy band to resolve the spectral features. These two requirements need to be fulfilled by an instrument with a detection sensitivity better than the previous ones in order to detect new objects and to improve the statistical significance of the known sources.

INTEGRAL [6] is a satellite mission for γ-ray astronomy which has been selected by ESA within the Horizon 2000 program. The two main instruments proposed for the payload of INTEGRAL are one optimized for spectroscopy and one for imaging. Both detectors are coupled with a coded mask. The INTEGRAL payload is completed by two monitors, one operating in the X-ray band (JEMX) and the other in the optical window (OMC).

The authors have been involved in the design of the Imager, which is addressed in Section 2 of this paper, and in the evaluation of its key performances (Section 3).

The INTEGRAL mission is actually under phase B studies, which implies that some changes on the instrument design have been produced after the phase A completion and some others changes will be expected on the near future. Nevertheless, we present here the results obtained for the baseline design assumed during phase A. Further studies are under development in order to improve the scientific performances of the Imager. In this context Monte Carlo instrument simulation seems to be a powerful tool, in order to model the Imager response when changes on its design are done.

---

[*] Corresponding author. Tel. +34 6 3864755.

PII S0168-583X(96)00726-4

2. The design of the Imager

The science requirements, which have been briefly outlined in the introduction, stressed the importance for the Imager of achieving at the same time good continuum sensitivity and fine angular resolution. In designing a satellite-borne telescope with such characteristics we should also bear in mind the limits of weight and power consumption given by the possible mission scenarios, which in our case are 630 kg, and 187 W, respectively.

In order to fulfill these requirements, the design of the Imager has been based on an instrument having: i) a good photopeak detection efficiency over the 50–5000 keV energy range, which implies a high atomic number, Z, and a high density material; ii) a low background counting rate, which is achievable by optimizing the (active and passive) shielding and the geometrical configuration of the detector as well as by a careful choice of the satellite orbit; iii) a position sensitive detector with an intrinsic spatial resolution of the order of 1 cm, coupled with a coded aperture mask.

In the case of scintillators, it is possible to use a position sensitive Anger-type gamma camera like that used in SIGMA [2], by means of a large single scintillator crystal. However the problem of a poor sensitivity induced by a loss of spatial resolution [4] arises in the low energy range due to the high background counting rate in a large single crystal at low energy. In addition, for an Anger camera the high energy sensitivity is limited by the thickness of the NaI crystal that cannot exceed ~ 15 mm in order not to make worse the above mentioned problem. Moreover, a detector having the capability of reconstructing the triggered detection element (and therefore the position with a good precision) for each interaction is preferable for background reduction purposes.

Since a 1–1 correspondence between the detection element and the light (charge) collector is more suitable, the chosen configuration is CsI(Tl) crystals viewed by silicon photodiodes (PD). CsI(Tl), with a density of 4.51 g cm^{-3} and $Z = 54$, has a high stopping power for γ-rays. CsI(Tl) has also the highest light output of all presently known scintillators, having a measured absolute scintillation yield of 64 800 photons/MeV for γ-rays at room temperature [7]. Moreover, the CsI(Tl) scintillation light is very well matched to the spectral sensitivity of silicon PIN PDs [8]. Valentine et al. [7] have calculated the expected external and internal wavelength-averaged quantum efficiencies for CsI(Tl) when coupled to a typical silicon PIN photodiode, obtaining about 70% and 90% respectively, slightly dependent on the temperature. The CsI(Tl)/PD system shows a higher electronic noise than a detector based on photomultipliers. This fact is negligible at high energies but raises the problem of the low energy threshold. One method to overcome this problem which is actually under consideration is to replace some CsI(Tl) elements by room temperature solid-state detectors (CdTe) with capabilities at low energies (down to 15 keV).

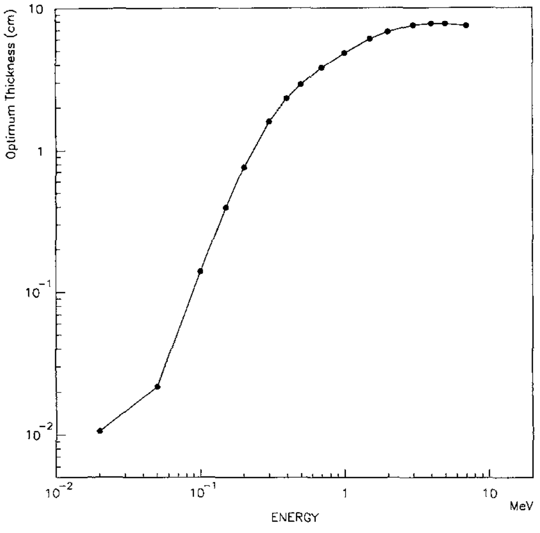

Fig. 1. Optimum thickness of CsI(Tl) as a function of energy.

Taking into account all the above considerations, the basic detector design is a large area array of discrete CsI(Tl) elements having a cross-sectional area of ~ 1 cm^2 each.

In order to evaluate the best thickness in terms of sensitivity, the following expression can be used:

$$S = \text{const.} \times \frac{\sqrt{B}}{\epsilon\sqrt{A}}, \qquad (1)$$

where ϵ is the detection efficiency, B represents the background counts, A the detection area and the constant includes all the other parameters (observing time, significance level, ...). Now, as a first approximation we can assume that B can be expressed as KV where K is a constant and V is the volume of the detector. If we consider also that the detection efficiency (ϵ) can be written as $1 - e^{-\mu t}$, μ being the linear absorption coefficient of the material (CsI(Tl) in our case) and t the thickness of the detector, Eq. (1) can be written as:

$$S = \text{const.} \times \frac{\sqrt{V}}{1 - e^{-\mu t}\sqrt{A}}. \qquad (2)$$

If we express the volume V as t^3, and the detection area A as t^2 (cubic approximation), we obtain:

$$S = \text{const.} \times \frac{\sqrt{t}}{1 - e^{-\mu t}}. \qquad (3)$$

If we plot the profile of S as a function of μt (Eq. (3)), the optimum value, i.e. the minimum value of S, is reached when μt is equal to 1.256. We can now find the optimum thickness as a function of energy $t(E)$, by plotting $1.256/\mu(E)$ vs. E (Fig. 1).

The final design of the detector has been based on a multilayer structure. This kind of vertical segmentation offers two major advantages: i) the sensitivity is improved, in particular at low energy, by optimizing the thickness of the different layers; ii) the detector can work at different independent

Table 1
Three-layer configuration selected for the INTEGRAL Imager

Layer	Thickness [cm]	Optimum energy
Top	1	250 keV
Centre	3	700 keV (4 cm)
Bottom	3	2-5 MeV (7 cm)

operative modes, allowing an optimization of the overall detection sensitivity.

In Table 1 the vertical geometrical structure of the detector is described and the energy values at which the sensitivity has been optimized for each layer is indicated. The main detector (Fig. 2) is then shielded on six sides and the bottom by 2 cm thick active BGO crystal, to reject photons not coming from the source field, and by a 0.6 cm thick plastic veto over the top, to reject signals caused by the interaction with charged particles.

For the production of images of the γ-ray sky, the "coded-mask" technique [9] is used. In coded-aperture imaging a mask with opaque and transparent elements is placed between the detector and the source. The image results from a deconvolution between the shadow produced on the detector and the pattern of the mask elements. The elements chosen for the Imager mask are made of tungsten ($Z = 74$) with a thickness of 1.5 cm, which represents a compromise between ideally opaque elements and the existing limits of weight. Several exhaustive papers exist which describe mathematical methods for the generation of optimum mask patterns [10], and this problem is not addressed to in our work. The geometry which was chosen for the mask pattern of the INTEGRAL Imager was based on hexagonal pixels; this choice was also the driver for the geometry of the detector which is constructed by an hexagonal array of 24 triangular modules with 120 hexagonal detection units in each module.

Table 2
Operative modes in the Imager detector

Mode	Number of interaction(s)/layer		
	1st layer	2nd layer	3rd layer
1a	1	–	–
1b	2	–	–
1c	> 2	–	–
2a	–	1	–
2b	–	2	–
2c	–	> 2	–
3a	–	–	1
3b	–	–	2
3c	–	–	> 2
4a	1	1	–
4b	1	> 1	–
4c	> 1	≥ 1	–
5a	1	–	1
5b	1	–	> 1
5c	> 1	–	≥ 1
6a	–	1	1
6b	–	1	> 1
6c	–	> 1	≥ 1
7a	1	1	1
7b	≥ 1	≥ 1	≥ 1

The multi-layer discrete elements geometrical assembly, provides the possibility for the detector to work in different independent operative modes, a feature, which, as it will be shown in Section 3, can give an improvement on the signal to noise ratio. The operative modes are defined according to the number and the location of the interaction(s) caused by the primary incident γ-ray; the 20 possible modes are indicated in Table 2.

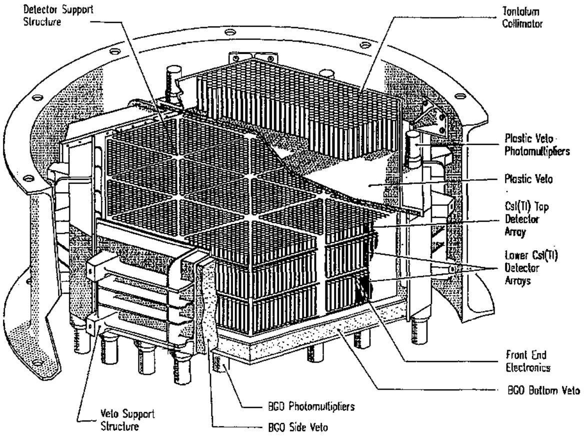

Fig. 2. INTEGRAL Imager detector assembly.

3. Evaluation of instrument capabilities and performance

A Monte Carlo simulation program based on the GEANT software package [11] has been implemented for the evaluation of the key scientific performances of the Imager, which are summarized as follows: the detection efficiency, the capability of reconstruction the incidence pixel for each event, the possible non-uniformity due to the complex geometrical arrangement, to the presence of passive material or to other factors, and the distribution of the order of multiplicity and adjacency for the different classes of events. In all the cases the calculations were done in such way that the primary photons were injected uniformly distributed over its top face, the incident direction being normal to the detector plane.

3.1. Detection efficiency

3.1.1. Monoenergetic sources

The results of calculations of the detection efficiency obtained for monoenergetic sources were reported in a previous paper [12]. Figs. 3-6 depict the results obtained for total and full-peak efficiencies at different incident photon energies, showing the contribution of the different opera-

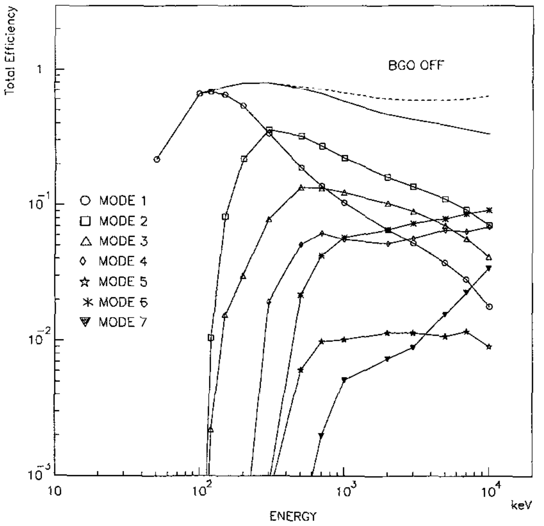

Fig. 3. Total detection efficiency for the Imager detector obtained by simulation, showing the contribution of the different operative modes. The effect of the BGO A/C "ON" (full line) and "OFF" (dashed line) veto shield are displayed.

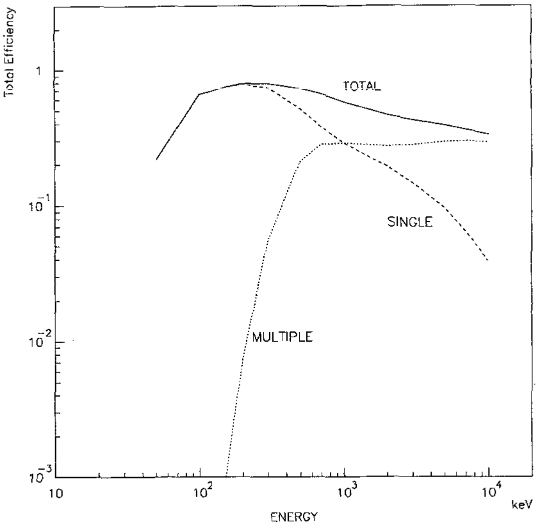

Fig. 5. Total detection efficiency for the Imager detector obtained by simulation, showing the contribution of single and multiple events.

tive modes considered (Table 2). In Fig. 3 the effect of the BGO veto is also displayed, its effect being negligible below 500 keV. Figs. 5 and 6 show single events (only one bar is triggered, modes 1a, 2a and 3a) dominate at incident energies below 1 MeV, whereas above that energy the multiple events (more than one bar is triggered) dominate.

The photopeak efficiency decreases rapidly above 600 keV. This behaviour is due to the effect of the upper energy threshold. The effect of both upper and lower thresholds, which are imposed by experimental conditions, will be discussed below.

It is very interesting to know the partial contribution of the different sub-modes to each operative mode. In Figs. 7 and 8 we present the contribution to the total efficiency of the different sub-modes considered. As the energy increases the contribution due to sub-modes with more than two bars triggered increases, the sub-modes corresponding to 1 or 2 bars triggered decrease.

As was already pointed out, the above calculations have been done taking into account the lower and upper energy thresholds, in order to simulate as much as possible the real conditions. In Figs. 9 and 10 we compare the results obtained

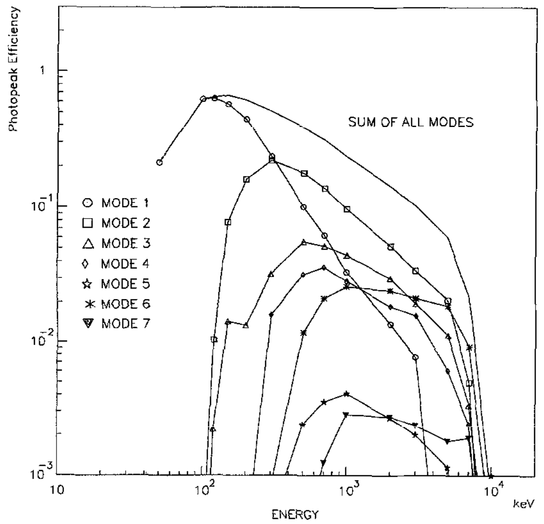

Fig. 4. Full-peak efficiency for the Imager detector obtained by simulation, showing the contribution of the different operative modes.

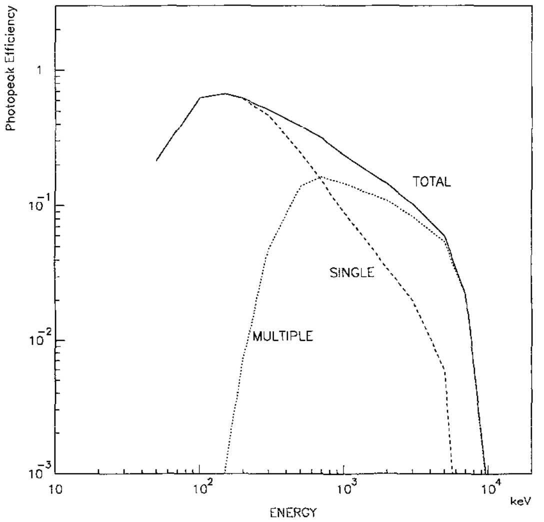

Fig. 6. Full-peak efficiency for the Imager detector obtained by simulation, showing the contribution of single and multiple events.

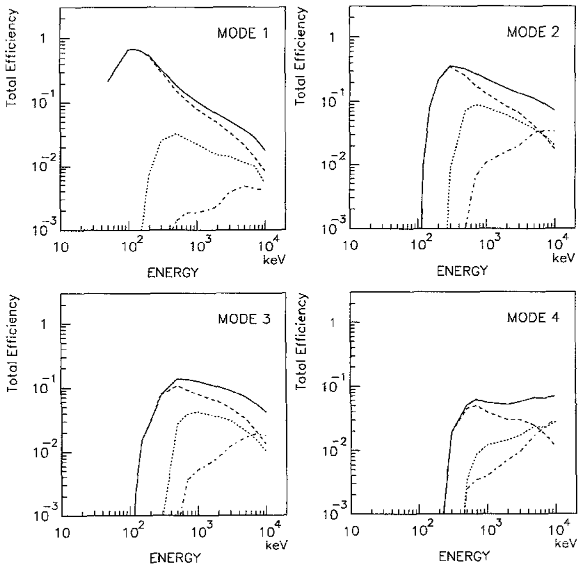

Fig. 7. Partial contribution to total efficiency of the Imager for the different sub-modes considered. Full line: total efficiency for the mode. Dashed line: total efficiency for sub-mode a. Dotted line: the same for sub-mode b. Dash-dotted line: the same for sub-mode c.

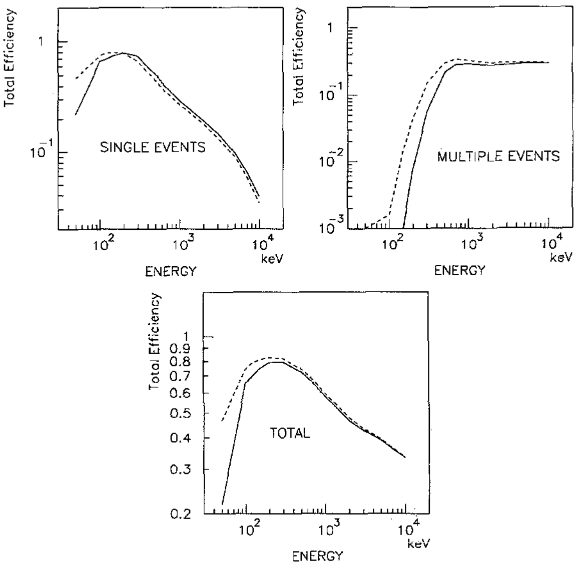

Fig. 9. Comparison of the results obtained by simulation for total efficiency with (full lines) and without (dashed lines) considering the energy thresholds for CsI bars.

by simulation for total- and full-peak efficiencies with (full lines) and without (dashed lines) consideration of the energy thresholds for CsI bars. In all cases the threshold energies for plastic and BGO veto shields were 40 and 100 keV respectively. The lower energy threshold for the CsI bars were 50 keV for the top layer and 120 keV for the centre and bottom layers, while the upper energy threshold was 3000 keV for the top layer and 6000 keV for centre and bottom layers. In order to maintain the maximum information, an energy deposit equal to the upper energy threshold was assigned to the corresponding CsI element when the energy deposit is greater than the assumed upper energy threshold.

In Fig. 9 it seems that the total efficiency for single events considering the energy thresholds is greater than without

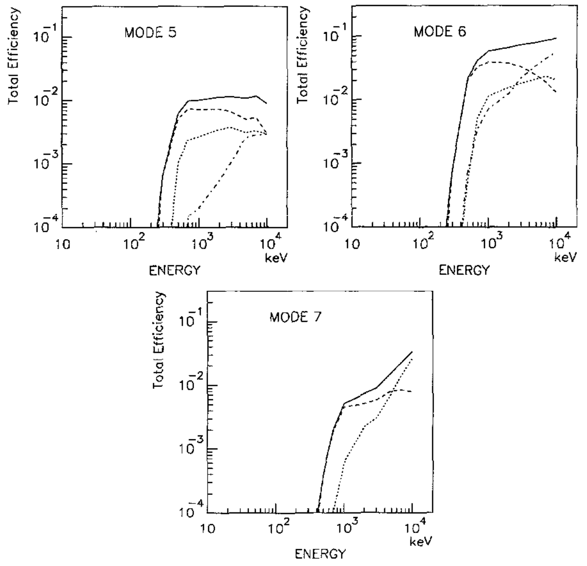

Fig. 8. Partial contribution to the total efficiency of the Imager for the different sub-modes considered. Full line: total efficiency for the mode. Dashed line: total efficiency for sub-mode a. Dotted line: the same for sub-mode b. Dash-dotted line: the same for sub-mode c.

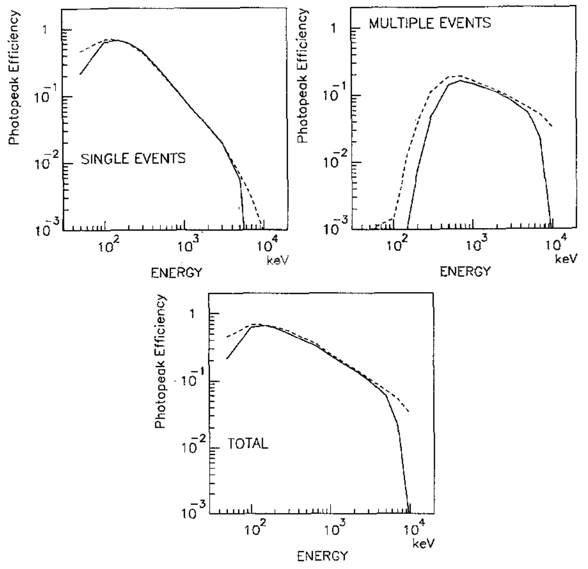

Fig. 10. Comparison of the results obtained by simulation for full-peak efficiency with (full lines) and without (dashed lines) considering the energy thresholds for CsI bars.

considering them. However, we must take into account the other component (multiple events) of the Imager detector in order to explain this behaviour: events which are accounted as single events (only one bar is triggered) when energy thresholds are taken into account could become multiple events when no energy thresholds are considered. Actually, for low energies, where the photon is expected to deposit nearly all its energy in one interaction, the single events detection efficiency (Fig. 9) without considering energy thresholds is greater than when they are taken into account.

In Fig. 10 it can be seen that the total photopeak efficiency decreases dramatically above 6000 keV when the energy thresholds are considered (the differences being negligible below this energy). The great differences correspond to multiple events, while for single events these differences are smaller. This behaviour for multiple events shows that for energies $\geq$ 6000 keV the photon deposits a high fraction of its energy in a single CsI bar, while the energy deposit in the other(s) crystal(s) triggered (multiple events) is much smaller.

3.1.2. Celestial sources

In the above calculations we have simulated the Imager response against ideal monoenergetic sources. However, it is important to study the Imager response when "illuminated" with photons which have a continuum energy distribution following the spectral law of a real celestial object.

In general, the power-law spectrum of such celestial sources in the gamma ray range can be described as follows:

$$\frac{\mathrm{d}N}{\mathrm{d}E} = KE^{-\alpha} \ (\text{photons}\,\text{cm}^{-2}\text{s}^{-1}\text{keV}^{-1}), \tag{4}$$

where N is the number of photons with energy E, K and α being constants depending on the source considered.

We have considered in our calculations two celestial objects: the Crab pulsar (assuming $K = 4.5$ and $\alpha = 2$) and the QSO 3C273 quasar ($K = 4 \times 10^{-2}$ and $\alpha = 1.6$). The expected response of the Imager detector together with the emission curves is shown in Fig. 11 (left). Single events dominate at energies below 700 keV, whereas the multiple events dominate above that energy. The upper energy threshold implies the appearance of two well-defined peaks at 3000 and 6000 keV. On the other hand, the lower energy thresholds for the second and third layer (120 keV) produce an increase in the Imager response for that energy. Note that for each energy the total number of events detected in the Imager is considered. In this sense the Compton continuum can produce (for a determined energy interval) a number of detected events greater than those emitted by the celestial object in the same energy interval. For these energies this fact implies that the efficiency is greater than 1 (Fig. 11, right). These efficiencies are defined (for a determined energy interval) as the ratio between the number of emitted photons by the celestial object and the total number of detected events in the Imager in the energy interval considered. The effect of the BGO veto is also displayed in Fig. 11 (right), its effect being negligible for energies below ≈ 500 keV (the same behaviour was observed for monoenergetic sources, Fig. 3).

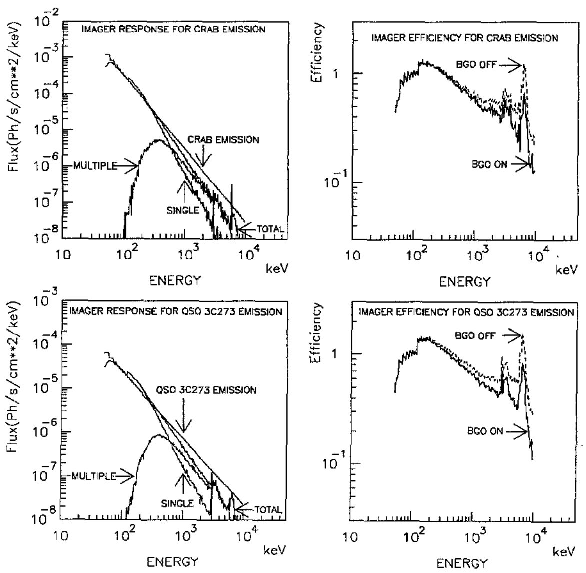

Fig. 11. Left: expected response of the Imager detector against the Crab pulsar (upper left) and QSO 3C273 quasar (bottom left) emissions. The assumed curve emissions of these celestial objects are also displayed. Right: expected efficiency of the Imager detector for Crab (upper right) and QSO 3C273 (bottom right) emission. The effect of the BGO veto shield is displayed.

3.2. Incidence pixel reconstruction capability

The quality of the shadowgram produced by the mask pattern depends upon the ability of the position sensitive detector to reconstruct the pixel of incidence for each primary photon (event). In the ideal situation the detector has a thickness $t = 0$ (and a detection efficiency $\varepsilon = 1$), so that the incidence pixel is obtained without ambiguity. In the real case different criteria have to be developed in order to assign to each multiple event the pixel through which the primary photon has first "entered" the detector.

For this purpose, we have envisaged the following criteria and tested them by simulation:

- *D1* (*minimum depth*): The incidence pixel is assumed to be the one triggered with the minimum depth interaction.
- *D2* (*maximum depth*): The incidence pixel is identified with the one at the maximum depth interaction.
- *E1* (*minimum energy deposit*): The incidence pixel is assumed to be the one triggered with the minimum energy deposit.
- *E2* (*maximum energy deposit*): The incidence pixel is identified as the one with the maximum energy deposit.

These techniques can be applied only for multiple events (for single events the incidence pixel is assumed the only one triggered). However, these criteria cannot be applied to

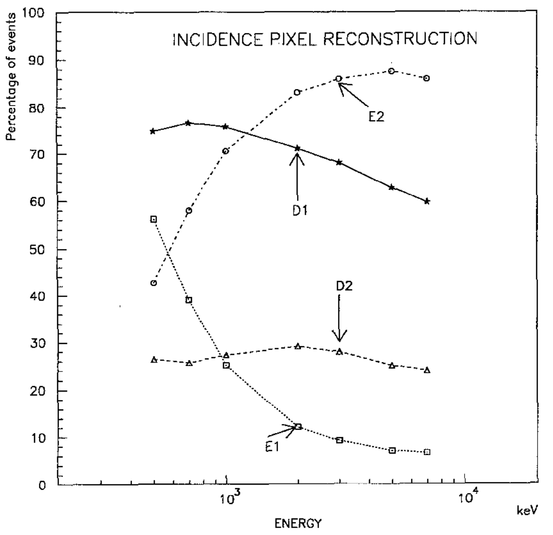

Fig. 12. Incidence pixel reconstruction ability of the Imager detector as a function of the incident energy for different criteria: D1: minimum depth. D2: maximum depth. E1: minimum energy deposit. E2: maximum energy deposit. (see text).

all operative multiple modes. Therefore we have considered three different types of events (A, B and C) according to the criterion that can be applied in each case:

- *Type A* (sub-modes 4a, 5a, 6a and 7a): D1, D2, E1 and E2 criteria are applicable.
- *Type B* (sub-modes 4b, 5b and 6b): D1, E1 and E2 criteria are applicable.
- *Type C* (sub-modes 1b, 1c, 2b, 2c, 3b, 3c, 4c, 5c, 6c and 7b): only E1 and E2 criteria are applicable.

Fig. 12 shows the incidence pixel reconstruction ability of the Imager detector as a function of the incident energy for the different criteria considered. The percentage of events whose incidence pixel has been correctly assigned is showed in the vertical axis. That percentage is calculated over the total number of events for which the considered technique is applicable.

At high energies it can be seen that the best criterion for any type of event is E2, but it is very energy dependent and fails for energies below 1000 keV. For energies below 1000 keV the best criterion is D1. In fact, this criterion is rather energy independent, but it is only applicable for type A and B events.

It is also very interesting to determine, when a criterion fails, the associated error in pixel units between the real incidence pixel and that one assigned by the criterion (point spread function). This is displayed in Fig. 13: given all the events in which the criterion has failed we show the percentage of them, at three different incident energies, having their true incidence pixel at a certain distance (in pixel units this distance is called adjacency) from the incidence pixel assigned by the criterion. The criterion assumed in each case was the most successful one for each energy.

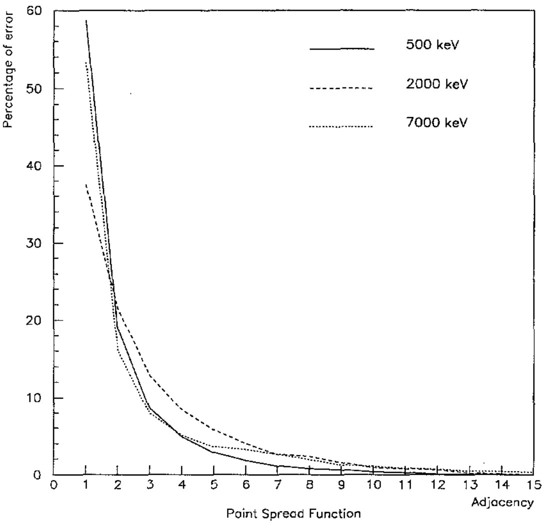

Fig. 13. Point spread function of the Imager detector for the incident pixel reconstruction technique. In each case the best criterion was used (see text).

It can be seen that between 40% and 60% of the events for which the criteria have failed are only at one pixel from the true one, and about 80% are included in a spatial region of two pixels around the real one.

In view of these results it can be concluded that the ability of the Imager to reconstruct the incidence pixel, using the techniques mentioned above, will allow to have a quite good quality of the shadowgram produced by the mask pattern.

3.3. Non-uniformity of the detection plane

Given the relatively complex structure of the instrument, it is important to verify possible variations of the detection efficiency across the detection plane. The active detection elements of the instrument constitute $\simeq$ 70% of the total Imager mass within the active shield, and the detection surface is $\simeq$ 68% of the total detector area. The rest consists of passive material like silicon PDs, Ni housings of the CsI(Tl) elements, Al supports of the triangular modules, and so on. In particular we have investigated the non-uniformity in the detection efficiency in the regions near the vertex of a triangular module, where the presence of passive material per unit area is greater. Fig. 14 displays the uniformity profile for single events of the six central triangular modules for an incident photon energy of 500 keV.

The uniformity of the detection efficiency across the detection plane has been studied both at the level of the whole hexagonal detector and at the level of the triangular modules. In the first case the variation of the detection efficiency has been registered as a function of position, from the central pixels, corresponding to the vertices of the six central triangular modules, moving outwards to the detector area corresponding to the central regions of the triangular modules, where the fraction of passive material becomes less impor-

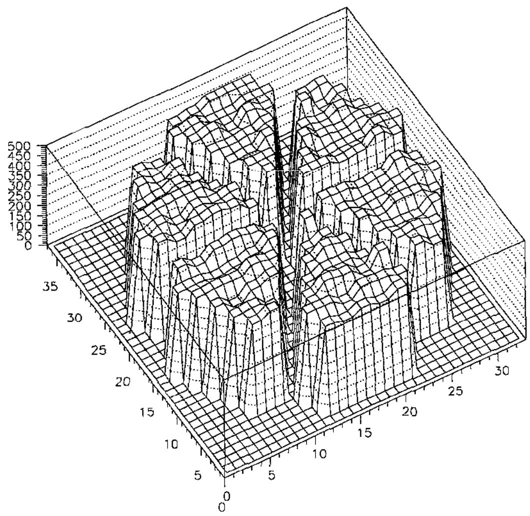

Fig. 14. Monte Carlo results obtained for the uniformity response of the six central triangular modules of the Imager for an incident photon energy of 500 keV. Only the single events profile is displayed.

tant, and therefore where the non-uniformity is expected to be less pronounced.

The results obtained by simulation for three different incident energies are listed in Table 3a. The values are normalized to the central regions of the triangular modules (1.00), far away from the vertices of the six central triangular modules which correspond to the first values in Table 3a. The non-uniformity is more pronounced at high energies for single events (≈ 25% at 2000 and 7000 keV in the extreme positions), being similar in the case of multiple events for the energies considered (≈ 20% in the extreme positions). However, as can be expected, the single and multiple events show an opposite trend. The increase in the multiple events detected as we move away from the vertices of the six central triangular modules is accompanied by a reduction in the single events detected. The same behaviour is observed in the case of triangular modules (Table 3b).

For the study of uniformity at the level of triangular modules, the variation of detection efficiency has been registered as a function of position across the area of each module, moving from the outer to the internal region. Once again the values are normalized to the inner region of the triangular module (Table 3b). In this case the non-uniformity shows a more pronounced dependence with the energy considered. As the energy increases, the lack of uniformity increases for single events and diminishes for multiple events. For single events the non-uniformity is greater than for multiple events showing a strong dependence with the region considered. It seems that the observed non-uniformity at triangular level is very high, making it necessary to study carefully the implications of these results on the Imager design.

Table 3
Uniformity study
(a) Distribution of events across the detection plane

Energy [keV]							
Single events							
500	1.06	1.07	1.05	1.03	1.04	1.02	1.00
2000	1.25	1.14	1.09	1.07	1.02	1.01	1.00
7000	1.24	1.12	1.12	1.08	1.04	1.03	1.00
Multiple events							
500	0.77	0.89	0.93	0.93	0.95	0.98	1.00
2000	0.78	0.87	0.90	0.96	0.95	0.98	1.00
7000	0.83	0.92	0.95	0.94	0.95	0.98	1.00

(b) Distribution of events in the triangular modules

Energy [keV]					
Single events					
500	1.25	1.10	1.04	1.01	1.00
2000	1.63	1.26	1.07	1.02	1.00
7000	2.38	1.50	1.17	1.11	1.00
Multiple events					
500	0.62	0.91	0.99	1.00	1.00
2000	0.66	0.81	0.89	0.92	1.00
7000	0.84	0.96	0.99	1.00	1.00

3.4. Distribution of multiplicity and adjacency order

Given the very high number of detection elements (2880 for each of the three layers) present in the instrument, it is very important to study the number and the location (in x, y and z) of the interactions determined by the primary gamma ray, as a function of their incident energy. This analysis can have significant consequences for what concerns the logic and the philosophy to be applied for the (anti)coincidence among signals coming only from the detection elements, and from both the detection elements and the veto system. Moreover, it is in principle possible to increase the signal to noise ratio by rejecting events according to their three-dimensional spatial characterization (i.e. the distribution of the triggered detection units).

To attend this, the adjacency order is defined as the maximum distance, expressed in number of detection elements, in any direction (horizontal, vertical and diagonal) among all the possible pairs of interaction for a given event.

In Fig. 15 is shown the distribution of the multiple events (in percentage over the total multiple events) obtained by simulation, according to their adjacency order for three different incident photon energies (300, 3000 and 7000 keV). As can be expected, the spatial dispersion of the signals increases as the energy increases. More interesting is to know the adjacency order needed to have a determined percentage of the whole multiple events as a function of the incident energy of the photons. In Fig. 16 the adjacency order as a function of the energy for 50, 75, 90, 95 and 99% of the multiple events included can be seen. It seems that the variation

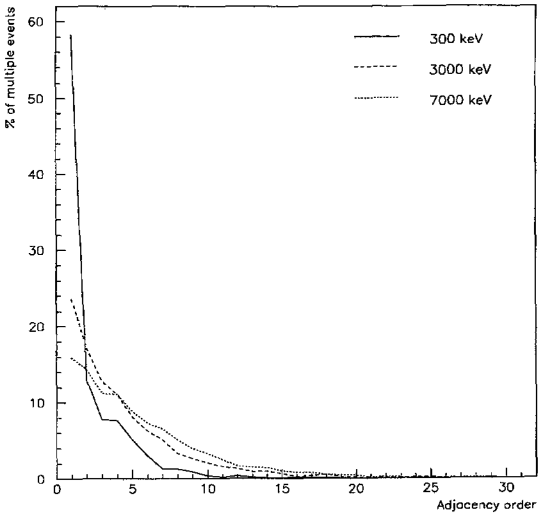

Fig. 15. Distribution of the multiple events (in percentage over the total multiple events) obtained by simulation, according to their adjacency order for three different incident photon energies.

with the energy of the adjacency order increases rapidly for energies below 2000 keV, this increase being slower above that energy.

Another important result is to establish the number of interactions determined by the primary photon, as a function of their incident energy. The multiplicity order is simply defined as the number of different detection units which have been triggered by at least one interaction caused by the primary photon. In Fig. 17 is shown the percentage of events as a function of the multiplicity order for different incident photon energies (0.5, 2, 5 and 10 MeV). As can be expected, the relative contribution of high multiplicity order events increases as the energy increases. On the other hand, the multiplicity order is always less than 10, and the 95% of the events have a multiplicity order less than 4 at 5 MeV.

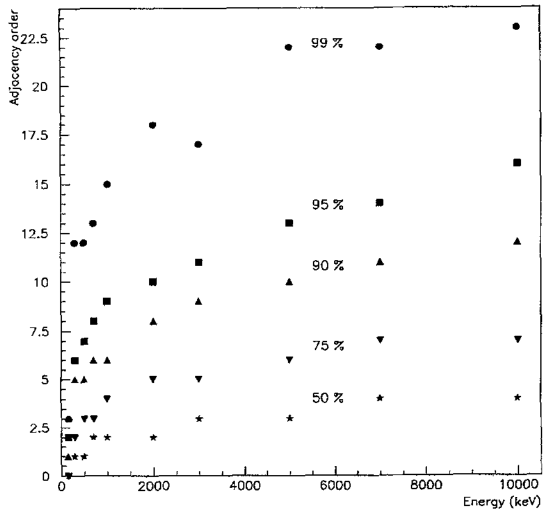

Fig. 16. Adjacency order as a function of the energy for 50, 75, 90, 95 and 99% of the multiple events included.

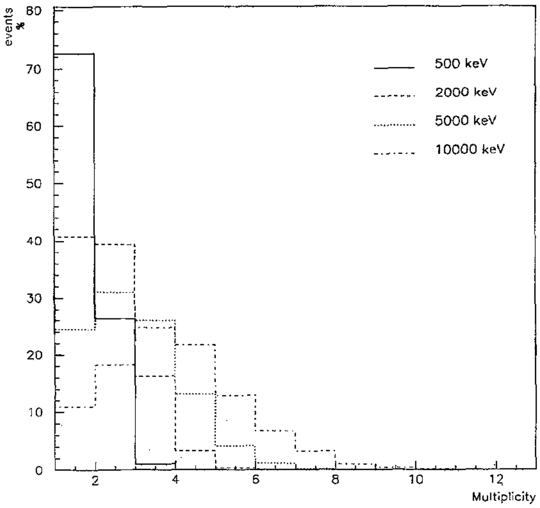

Fig. 17. Distribution of the events (in percentage) obtained by simulation, according to their multiplicity order for different incident photon energies.

This kind of information is of great importance because it can be used to reject events which are not in accordance with these results. In this sense a improvement in the signal to noise ratio can be achieved by using this information.

4. Conclusions

The Imager is one of the main instruments under development for the INTEGRAL payload devoted to fine imaging of astronomical γ-ray sources.

The phase A baseline design of the INTEGRAL Imager has been discussed and its main performances have been evaluated by Monte Carlo simulation, using the GEANT-3 package. The knowledge of the response of the instrument allows us to optimize the design and at the same time to define the logic and philosophy to be applied for the signals coming from the detection elements. By using this information it is also possible to increase the signal to noise ratio by rejecting events not coming from the celestial sources under study (for example according to their three-dimensional spatial characterization by means of the information obtained from the distribution of multiplicity and adjacency order of "true" events).

The INTEGRAL mission is actually under phase B studies. The possibility to extend the energy response of the Imager at low energies (down to 15 keV), by replacing the first CsI layer by CdTe solid state detectors is now considered as baseline. However, the INTEGRAL Imager design is not yet frozen and further studies are under development in order to improve the scientific performances of the instrument.

Acknowledgement

This work has been supported by the Spanish Comisión Interministerial de Ciencia y Tecnología under grant ESP-93-0754-CO3-01.

References

[1] N. Gehrels, Proc. 3rd Compton Symp. on Gamma-Ray Astronomy and Astrophysics, June 1995, Munich, Germany, in press.
[2] P. Mandrou et al., Astrophys. J. Suppl. 92 (1994) 343.
[3] A. Goldwurm et al., Nature 371 (1994) 589.
[4] L. Bassani and G. Di Cocco (eds.), Proc. Int. Workshop on Imaging in High Energy Astronomy, September 1994, Capri, Italy.
[5] P. Mandrou et al., Astron. Astrophys. Suppl. Ser. 97 (1993) 1.
[6] S. Bergeson-Willis et al., INTEGRAL Phase-A Report, ESA SCI(93)I, 1993.
[7] J.D. Valentine, W.W. Moses, S.E. Derenzo, D.K. Wehe and G.F. Knoll, Nucl. Instr. and Meth. A 325 (1993) 147.
[8] H. Grassmann, E. Lorenz and H.-G. Moser, Nucl. Instr. and Meth. A 228 (1985) 323.
[9] E.E. Fenimore and T.M. Cannon. Appl. Optics 17 (1978) 337.
[10] E. Caroli et al., Space Sci. Rev. 45 (1987) 349.
[11] R. Brun, F. Bruyant, M. Mairie, A. C. Mcperson and P. Zanarini, Data Handling Division CERN, DD/EE/84-1 (1987).
[12] F. Sánchez, F. J. Ballesteros, V. Reglero, G. Malaguti and G. Di Cocco, Experimental Astronomy 6 (1995) 271.